Sustainable Horizons 9 (2024) 100093

Contents lists available at ScienceDirect

Sustainable Horizons

journal homepage: www.elsevier.com/locate/horiz

Critical Reviews

Advanced lithium ion-sieves for sustainable lithium recovery from brines

Qian Chen [a], Zhijie Chen [b,*], Hongqiang Li [c], Bing-Jie Ni [b,*]

[a] School of Civil and Environmental Engineering, University of Technology Sydney (UTS), City Campus, Broadway, NSW 2007, Australia
[b] School of Civil and Environmental Engineering, The University of New South Wales, Sydney, NSW 2052, Australia
[c] School of Resource and Safety Engineering, Wuhan Institute of Technology, Wuhan 430205, China

ARTICLE INFO

Keywords:
Lithium recovery
Lithium ion-sieves
Heteroatom doping
Stability selectivity
Adsorption behavior

ABSTRACT

The escalating demand for lithium in electrochemical energy advice has stimulated growing focus on extracting Li from alternative sources such as brines. Lithium ion-sieves (LISs), comprising manganese-based and titanium-based LISs, emerging as a promising Li recovery technique, attributed to their exceptional capacity for lithium uptake, selectivity, and recyclability. However, practical implementation faces two critical challenges: the potential dissolution of specific ions (e.g., Mn^{3+} and Ti^{4+}) and the severe particle aggregation during synthesis. In addition, coexisting ions like Mg^{2+} hinder the selective adsorption of Li^+ due to their similar chemical properties. To meet these challenges, heteroatom doping is supposed to enhance the performance of LISs and diverse heteroatom doped LISs have been developed recently. Herein, this comprehensive review begins by delving into the fundamental aspects of LISs, including the LIS effect and types of LISs. Subsequently, adsorption behavior and practical application of modified LISs were discussed. Finally, prospects and research directions to solidify the role of LISs in pioneering environmentally friendly and economically viable lithium recovery methods are outlined.

1. Introduction

Lithium, as the lightest alkali metal, exhibits a compelling array of chemical properties, including remarkable electrochemical activity and a high redox potential value. These unique attributes render it indispensable in numerous industries, spanning from the pivotal role it plays in the fabrication of lithium and lithium-ion batteries (LIBs) to its contributions in ceramic glass, nuclear fusion, pharmaceuticals, adhesives, lubricant grease, cement, and electrode welding (European Commission, 2023; U.S. Geological Survey, 2023). Given the current revolution in electric automobiles and electronic products, the demand for LIBs has reached unprecedented levels. In anticipation of an ever-growing market share for lightweight LIB-powered light vehicles and hybrid vehicles, securing a reliable supply of lithium through efficient extraction methods has become a matter of utmost importance to fulfill the strong and escalating market demand (Zeng et al., 2019).

There are two primary classifications for lithium resources: one comprises solid sources such as mineral ores (spodumene, petalite, lepidolite, amblygonite, zabuyelite, zinnwaldite, and eucryptite) (Karrech et al., 2020), and recycled LIBs (Zhang et al., 2023a; Yang et al., 2023), while the other encompasses liquid sources like salt-lake brine (Zhang et al., 2023b; Foo et al., 2023), geothermal brine (Mends and Chu, 2023; Kölbel et al., 2023), seawater (Aljarrah et al., 2023), and lithium electrolytes (Xu et al., 2023). Currently, commercial lithium production primarily relies on continental brines, which represent the most substantial resource accounting for 59% of global production (Swain, 2017). Consequently, there has been a growing trend towards extracting lithium from brines due to their greater availability. However, the recovery of lithium from brines continues to be a significant of interest and challenge. The coexistence of low Li^+ concentrations with high levels of interfering ions (e.g., Mg^{2+}, Ca^{2+}, Na^+, and K^+) poses a considerable hindrance to achieving efficient and environmentally friendly lithium extraction processes, especially for Mg^{2+} (Ji et al., 2018), which possesses the similar ionic hydration radius and chemical characteristics to Li^+, seriously affecting the separation efficiency (Zhang et al., 2024; Wang et al., 2024).

To date, various methods have been employed to extract lithium from brines, including evaporitic technology (Vera et al., 2023), chemical precipitation (Zhang et al., 2023c), solvent extraction (Li et al., 2023), and adsorption (Reich et al., 2023). Among them, the adsorption method stands out due to its cost-effectiveness, wide adaptability, and straightforward implementation. Lithium ion-sieves (LISs) represent a

---

* Corresponding authors.
E-mail addresses: Zhijie.Chen1@unsw.edu.au (Z. Chen), bingjieni@gmail.com (B.-J. Ni).

https://doi.org/10.1016/j.horiz.2024.100093
Received 26 November 2023; Received in revised form 21 January 2024; Accepted 23 January 2024

specialized category of lithium-selective adsorbents, characterized by distinctive chemical structures that enable the effective separation of Li^+ from brines (Wang et al., 2024; Meng et al., 2024). Over the past few decades, LISs technology has emerged as a leading methodology for lithium recovery from aqueous environments (Long et al., 2024). This approach provides an innovative and efficient way to extract lithium from complex solutions containing a multitude of coexisting ions such as Na^+, Mg^{2+}, K^+, and Ca^{2+}. The intrinsic lithium selectivity of LISs facilitates the production of high-purity lithium products with ease, rendering the technology particularly efficacious in lithium separation. This attributes a distinct advantage to LISs over other available technologies, underscoring its superiority in terms of efficiency and effectiveness in lithium extraction.

The constituents of LISs can be principally divided into two categories: lithium manganese oxides (LMO) and lithium titanium oxides (LTO) (Orooji et al., 2022). LMO is noted for its outstanding lithium affinity, superior adsorption capacity, and excellent regeneration performance, making it a promising candidate for lithium extraction. However, its inherent spinel structure is susceptible to manganese dissolution (Ryu et al., 2019; Noerochim et al., 2015), potentially diminishing its adsorption efficiency and leading to environmental risks. Conversely, LTO demonstrates exceptional structural stability, attributed to its high titanium-oxygen bond energy which effectively suppresses titanium dissolution. However, the adsorption performance of LTO is affected by particle aggregation during high temperature synthesis and its utility in lithium recovery from brines is significantly compromised when an electrical potential is applied (Zhang et al., 2014; Wei et al., 2020). These identified limitations represent critical challenges that must be addressed to enhance the performance and commercial viability of these materials in lithium extraction applications. Further research is anticipated to focus on mitigating these issues, paving the wat for broader commercial implementation.

Heteroatom doping provides several advantages to LISs. First and foremost, doping can enhance the stability and durability of materials, making it less vulnerable to degradation or damage (Qian et al., 2020a; Qian et al., 2021a; Xu et al., 2016). This feature is particularly crucial for practical applications that require the material to withstand harsh conditions. Secondly, doping can enhance the adsorption performance of LISs, allowing for more efficient and effective extraction of lithium from brines (Han et al., 2022). Thirdly, doping can also improve the selectivity of LISs, enabling more targeted extraction of lithium without interfering with other ions in the brine (Wang et al., 2018a). Doping technologies typically employed for LISs are classified into three categories: cation doping (Bao et al., 2022; Wang et al., 2022), anion doping (Qian et al., 2020b; Zhang et al., 2021), and co-doping (Han et al., 2022; Zhang et al., 2022). These strategies involve the partial substitution of metallic ions such as Li^+, Mn^{3+}, and Ti^{4+} in the LISs structure with other cationic ions of differing valence, or the replacement of O^{2-} ions with other anions. The performance and structural stability of doped LISs derivatives surpass those of undoped LISs, making them suitable for wider application in various water resources. To date, no comprehensive review has addressed the role of heteroatom doping technology in enhancing the adsorption performance of LISs or elucidated the relationship between the structure and adsorption performance of doped LISs.

In this review, we offer a thorough examination of the recent advancements in heteroatom doped LISs for Li^+ recovery from brines. Initially, we delve into the fundamentals of LISs, discussing the LISs effect and types of LISs. We subsequently outline the heteroatom doped LMO and LTO, placing particular emphasis on the structure-performance correlation of heteroatom doped LISs. The discussion then extends to adsorption behaviors and practical applications. Finally, we identify present challenges and forecast prospects, aiming to steer the creation of the next generation of high-performance adsorbents.

2. Fundamentals of LISs

2.1. LISs effect

The constituents of LISs can be principally divided into two categories: LMO and LTO. Following the ion exchange between Li and H (LMO and LTO are generally immersed in an acid solution like HCl to finish the ion exchange process), they transform into HMO and HTO, respectively. The ion sieve oxides, resulting from precursors incorporating the targeted metal ions, exhibit a unique affinity for those specific metal ions, primarily due to their ion screening capabilities. It is critical to highlight that the crystal structures of the precursor maintain relative stable since the vacant crystal sites can still be preserved following the extraction of the targeted metal ions. As such, the newly generated vacancies in the crystal can accommodate ions possessing ionic radii either equivalent to or smaller than those of the intended ions. In the context of LISs, Li^+ ion is the targeted ion and is initially extracted from the spinel structure, creating empty crystal sites that only allow Li^+ ions to reoccupy. This specificity arises because other coexisting ions possess larger ionic radii, inhibiting their ability to occupy the vacant sites. Fig. 1 illustrates the precise steps of the LISs effect: Initially, the hydrogen-filled state LISs [LIS(H)] is formed through the Li-H ion exchange when [LIS (Li)] is submerged in an acidic solution. Subsequently, lithium ions from the aqueous solution can preferentially occupy the created vacancies, whereas other coexisting ions such as Na^+, K^+, Ca^{2+}, and Mg^{2+} face resistance due to steric effects. Finally, after selective lithium adsorption, [LIS(H)] is transformed into [LIS(Li)], completing the process known as the LISs effect (Xu et al., 2016; Weng et al., 2020).

2.2. LMO

LMO is a type of LISs characterized by a spinel structure (Fig. 2). Within this structure, Li, Mn, and O are respectively located at tetrahedral sites (8a), octahedral sites (16d), and face-centered cubic sites (32e). It has been documented that the spinel structure comprises 32 octahedral gaps (16d), with approximately half of the crystal sites occupied by 32 oxygen atoms and 16 Mn atoms. The remaining crystal sites (16c) are unoccupied, thereby facilitating the migration of lithium ions situated at 1/8th of the 64 tetrahedral sites (8a) through the 8a-16c-8a route (Zhang et al., 2014; Wei et al., 2020; Qian et al., 2020a; Qian et al., 2021a; Xu et al., 2016).

The adsorption mechanism of LMO toward Li^+ can be categorized into three principal forms: oxidation–reduction, ion exchange, and a combined mechanism. The corresponding equations are represented as follows (Xu et al., 2016):

$$2(Li^+)Mn^{3+}Mn^{4+}O_4 + 4H^+ \rightarrow 1.5(\blacksquare)\left[Mn_2^{4+}\right]O_4 + 2Li^+ + Mn^{2+} + 2H_2O \tag{1}$$

$$(\blacksquare)\left[Mn_2^{4+}\right]O_4 + Li^+ + OH^- \rightarrow (Li^+)\left[Mn^{3+}Mn^{4+}\right]O_4 + 0.5H_2O + 0.25O_2 \tag{2}$$

$$(Li^+)\left[Mn^{3+}Mn^{4+}\right]O_4 + H^+ \rightarrow (H)\left[Mn^{3+}Mn^{4+}\right]O_4 + Li^+ \tag{3}$$

Eqs.(1) and (2) are attributable to the oxidation–reduction mechanism, while Eq.(3) is ascribed to ion exchange. A combined reaction mechanism suggests that both oxidation–reduction and ion exchange processes occur concurrently. Within these equations, the symbols (), [], and ■ denote the 8a tetrahedral site, 16d octahedral site, and vacancy, respectively. Fig. 3 provides insights into the reactions involved in lithium extraction and insertion in spinel manganese oxides.

Based on Eqs.(1) and (2), it is observable that superficial Mn^{3+} undergoes conversion to Mn^{4+} and Mn^{2+} during the Li-H exchange process. The Mn^{4+} remains stable within the spinel structure, forming λ-MnO_2, whereas Mn^{2+} tends to dissolve in the acid solution (HCl is generally used to finish the Li-H exchange process). The generation of Mn^{2+} in an aqueous solution can significantly deteriorate the spinel structure, consequently impacting its recyclability and adsorption capacity. Given

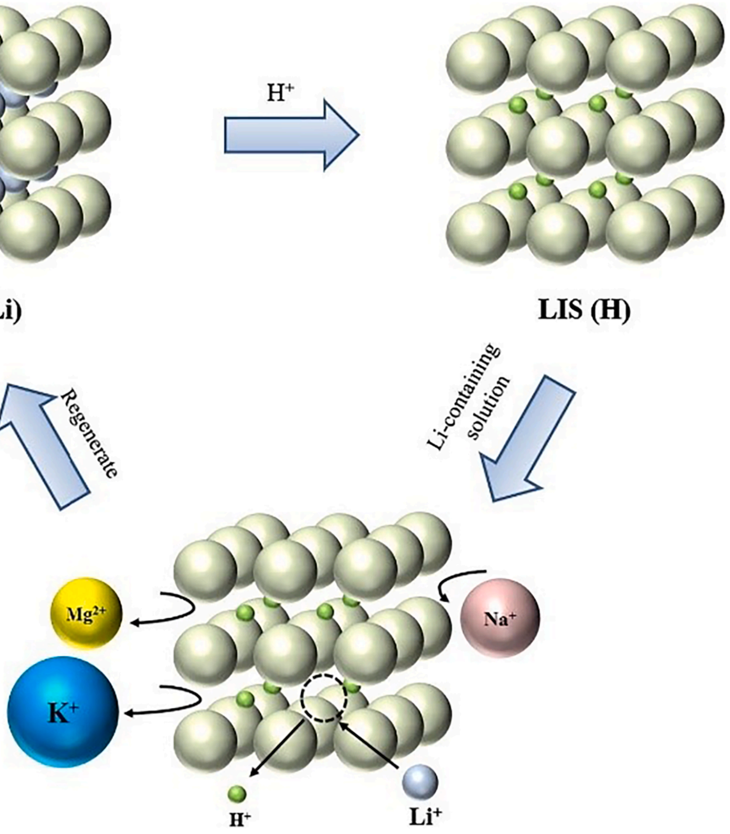

Fig. 1. Schematic representation of LISs process (The silver circle represents the Li^+ and the green circle represents the H^+) Xu et al., 2016.

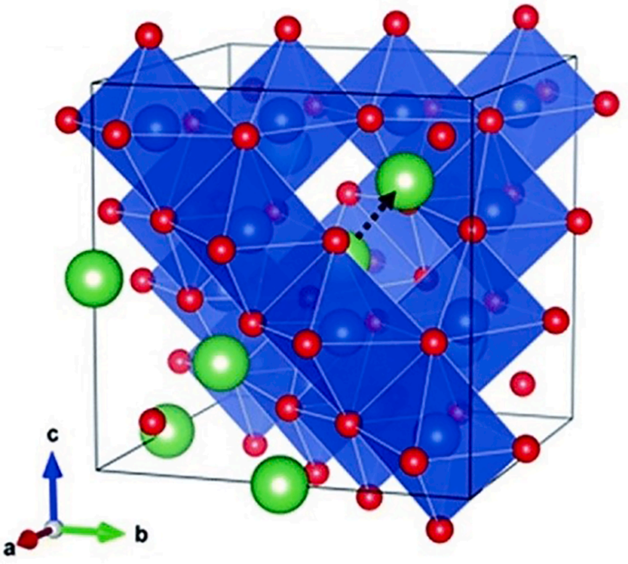

Fig. 2. Crystal structure of spinel $LiMn_2O_4$ (The red circle represents the oxygen, the green circle represents the lithium, and the blue octahedron represents the manganese) (Xiao et al., 2018).

these challenges, numerous variants of LMO-based LISs with superior adsorption capacities and stability have been developed. These include λ-MnO_2, $MnO_2·0·3H_2O$, and $MnO_2·0·5H_2O$, derived from the precursors of $LiMn_2O_4$, $Li_{1.33}Mn_{1.67}O_4$ ($Li_4Mn_5O_{12}$), and $Li_{1.6}Mn_{1.6}O_4$ ($Li_2Mn_2O_5$), respectively. $Li_{1.6}Mn_{1.6}O_4$ and $Li_4Mn_5O_{12}$ have garnered significant attention, as the tetravalent Mn valence in both spinel structures effectively hinders the disproportionation reaction of trivalent Mn, thus enhancing stability and adsorption capacity (Han et al., 2022; Wang et al., 2018). Empirical evidence (Table 1, the detailed calculation methods were described by Zhang et al. (2022). suggests that the theoretical adsorption capacity of various adsorbents correlates with the Li/Mn molar ratio, indicating that $MnO_2·0·5H_2O$ is the LISs with the highest theoretical adsorption capacity among the three types of LMO. Nevertheless, in practical applications, the adsorption capacity often falls short of the theoretical prediction, and the dissolution phenomenon remains inevitable.

2.3. LTO

LTO based LISs are primarily composed of Li_2TiO_3 and $Li_4Ti_5O_{12}$. The former exhibits a layered structure (Fig. 4a), while the latter is characterized by a spinel structure (Fig. 4b). The adsorption mechanism of $Li_4Ti_5O_{12}$ bears resemblance to that of LMO, as both conform to a spinel structure. Despite the limited accessibility of LTO-type LISs, there exists substantial potential to cultivate these environmentally friendly lithium adsorbents for industrial applications. LTO possesses notable advantages, including posing no risk to water quality and, importantly, exhibiting superior structural stability compared to LMO, which benefits long-term operation.

H_2TiO_3, characterized by a layered structure, originates from layered Li_2TiO_3 precursors. The crystal structure of this precursor can be accurately represented as $Li[Li_{1/3}Ti_{2/3}]O_2$. Evidence suggests the existence of two types of layers in the Li_2TiO_3 structure. The first layer, referred to as the Li layer, is solely constituted by lithium atoms, accounting for 75% of the total atomic composition. In contrast, the second layer (the $LiTi_2$ layer) primarily comprises 1/3 lithium atoms and 2/3 titanium atoms, with the lithium atoms in this layer constituting the remaining 25% of the total atomic composition (Xu et al., 2016).

It is important to highlight that following acid pickling (HCl is the predominant acid used for LTO acid pickling process), the lithium atoms

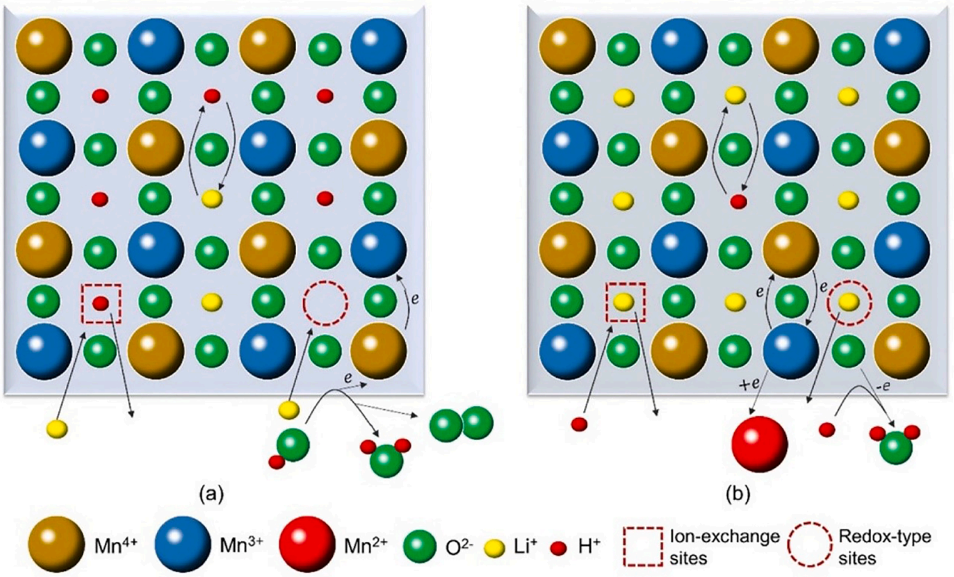

Fig. 3. Lithium (a) extraction and (b) insertion reactions in spinel manganese oxides (Liu et al., 2019).

Table 1
Adsorption capacity of different types of LMO.

Precursors	Ion sieve	Adsorption capacity, mg·g^{-1}	Ref
$LiMn_2O_4$	λ-MnO_2	39.7	(Zhang et al., 2022)
$Li_{1.33}Mn_{1.67}O_4$	$MnO_2·0·3H_2O$	58.8	
$Li_{1.6}Mn_{1.6}O_4$	$MnO_2·0·5H_2O$	72.3	

in both the Li layer and $LiTi_2$ layer can be entirely replaced by protons to form the H layer and HTi_2 layer, respectively. However, only the protons in the H layer can engage in further exchange with Li atoms in an aqueous solution to form a Li layer. In contrast, the protons in the HTi_2 layer maintain their structure without any alterations and do not participate in the subsequent exchange process. The lower adsorption capacity of H_2TiO_3, compared to its theoretical value, is primarily due to the inactive nature of the HTi_2 layers. The adsorption mechanism can be described by the following equations:

$$Li\left[Li_{\frac{1}{3}}Ti_{\frac{2}{3}}\right]O_2 + H^+ \rightarrow H\left[Li_{\frac{1}{3}}Ti_{\frac{2}{3}}\right]O_2 + Li^+ \tag{4}$$

$$Li\left[Li_{\frac{1}{3}}Ti_{\frac{2}{3}}\right]O_2 + \frac{1}{3}H^+ \rightarrow H\left[H_{\frac{1}{3}}Ti_{\frac{2}{3}}\right]O_2 + \frac{1}{3}Li^+ \tag{5}$$

$$Li\left[H_{\frac{1}{3}}Ti_{\frac{2}{3}}\right]O_2 + xLi^+ \rightarrow H_{1-x}Li_x\left[H_{\frac{1}{3}}Ti_{\frac{2}{3}}\right]O_2 + xH^+ \tag{6}$$

The selective adsorption of lithium over other coexisting ions is a result of the unique ability of lithium ions in an aqueous solution to selectively navigate through layered gaps and occupy exchange sites compared to competing ions such as K^+, Na^+, Ca^{2+}, and Mg^{2+}. This selectivity arises from the fact that ions such as K^+ (0.138 nm), Na^+ (0.102 nm), and Ca^{2+} (0.100 nm) have larger ionic radii than Li^+ (0.074 nm) and thus are unable to traverse the narrow channels. Although Mg^{2+} (0.072 nm) has a similar ionic radius to Li^+, the four-fold increase in free energy of hydration for Mg, compared to Li, significantly inhibits its dehydration, thereby restricting its ability to access the exchange sites.

Contrary to the generally accepted adsorption mechanism discussed earlier, a novel perspective was proposed by Marthi et al. (2021) (Fig. 5). They suggested that lithium adsorption involves two distinct types of O—H groups: isolated O—H groups and hydrogen-bonded O—H groups. In this process, surface O—H bonds are disrupted, leading to the formation of Li-O bonds. Notably, the isolated O—H groups, which derive from the HTi_2 layers, are anticipated to react more vigorously than the hydrogen-bonded O—H groups. This highlights the participatory role of the HTi_2 layers in lithium adsorption. Moreover, the exposure of HTi_2 layers could be enhanced through various methods, such as modifying the synthesis pathways or introducing dopants (Wang et al., 2016).

There are three types of Li_2TiO_3 including α-Li_2TiO_3, β-Li_2TiO_3, and γ-Li_2TiO_3. At synthetic temperatures below 300 °C, the metastable cubic α-Li_2TiO_3 phase predominates. This form transitions to the monoclinic β-Li_2TiO_3 phase as the temperature rises. When heated to 1155 °C or

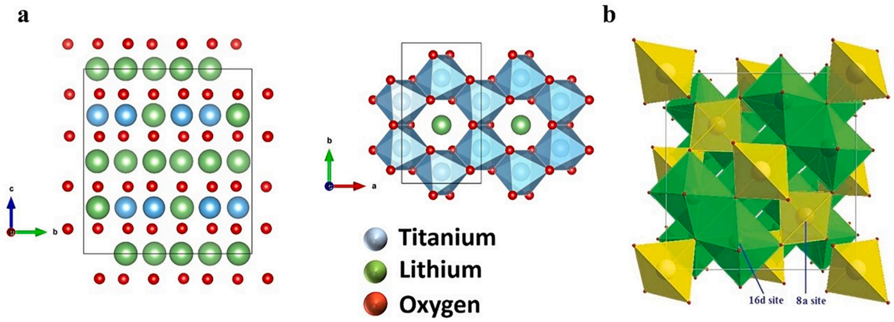

Fig. 4. Crystal structure of (a) Li_2TiO_3; and (b) $Li_4Ti_5O_{12}$ (Yellow tetrahedra represent lithium, and green octahedra represent disordered lithium and titanium) (Sun et al., 2015; Marthi et al., 2021).

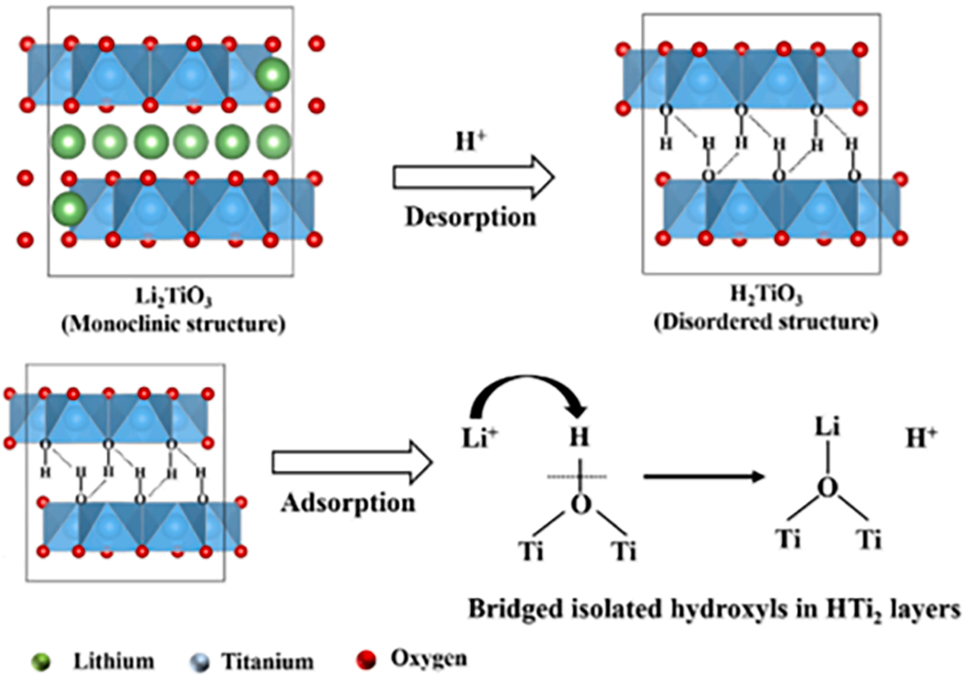

Fig. 5. Proposed lithium adsorption mechanism model based on bond breakage and bond formation (Marthi et al., 2021).

above, the majority form becomes γ- Li_2TiO_3. It has been observed that Li-H exchange efficiency is closely tied to the structure of the material. Specifically, monoclinic β-Li_2TiO_3, synthesized under 700 °C, exhibits a superior exchange rate of lithium and protons compared to cubic γ-Li_2TiO_3. This suggests that the β-Li_2TiO_3 structure has a greater number of generated vacant crystal sites available for lithium attachment (Zhou et al., 2017; Kang et al., 2022; Monchak et al., 2016).

3. Advanced heteroatom doped LISs for Li^+ adsorption

The synthesis of LISs is predominantly carried out through two main methods: solid-state reactions and hydrothermal reactions. The choice of method often depends on the specific material being synthesized. For LMO, hydrothermal reactions are commonly preferred, whereas for LTO, solid-state reactions are more frequently employed.

The conventional solid-state reaction method is known for its simplicity and ease of execution. However, this technique can result in non-uniform contact and incomplete reactions among the raw materials. Such issues often lead to the production of powders with large and unevenly distributed particle sizes. Additionally, solid-state reactions are generally time-consuming and energy intensive.

In the case of LMO, a significant concern is the dissolution of Mn^{3+} ions. This challenge impacts not only the recyclability and adsorption efficiency of the material but also raises environmental concerns due to the potential release of Mn^{3+} ions into aquatic ecosystems. Therefore, addressing these issues is crucial to improving the effectiveness, environmental compatibility, and overall sustainability of LIS adsorbents. In the subsequent sections, the focus will be on a detailed examination and discussion of doping-modified advanced LMO and LTO adsorbents, specifically designed for Li^+ adsorption. This comprehensive analysis will encompass various aspects of the doped LMO and LTO materials, including their structural modifications through doping and the resultant effects on their Li^+ adsorption capabilities.

3.1. *Doping-modified advanced LMO for Li^+ adsorption*

In the realm of heteroatom doping for modified LMO, the elements replaced by doped ions of varying valences differ, leading to distinct underlying mechanisms. For doping with monovalent and multivalent cations, the lithium and manganese elements in the LMO structure are the primary targets for substitution. Conversely, for anion doping, oxygen is the predominant element substituted. The aim of doping modification is to bolster the structural stability and enhance the adsorption performance of LMO. To this end, the incorporated ions should contribute positively to the stability of the structure.

There are essentially two strategies to enhance the stability of LMO. The first involves introducing ions that foster more durable and robust chemical bonds. This reinforcement enables the spinel structure to retain a degree of stability during the acidic exchange process and the high salinity adsorption process, thereby diminishing the dissolution rate of Mn^{3+} ions. The second strategy revolves around modifying the overall valence state of the LMO by introducing ions, which reduces the proportion of Mn^{3+} ions within the structure. This modification mitigates the disproportionation reactions that can occur during the adsorption process.

In this context, researchers have explored the doping of $LiMn_2O_4$ and $Li_{1.6}Mn_{1.6}O_4$ substrates. The aim is to replace specific elements in the spinel structure with ions of different valences to enhance the performance of LMO. The primary monovalent elements used for doping include sodium (Na^+) (Qian et al., 2021a) and potassium (K^+) (Qian et al., 2020a), while multivalent elements encompass magnesium (Mg^{2+}) (Bao et al., 2022), gallium (Ga^{3+}) (Ju et al., 2022), zirconium (Zr^{4+}) (Wang et al., 2022), aluminum (Al^{3+}) (Qian et al., 2021b; Chen et al., 2018; Zhang et al., 2019), iron (Fe^{3+}) (Gao et al., 2021), and chromium (Cr^{3+}) (Cao et al., 2019). The effect of multivalent element doping largely hinges on the ionic radius differential between the dopant and the manganese ion. A larger ionic radius can lead to crystal expansion, which increases pore size and thereby facilitates the adsorption process. Conversely, a smaller radius can result in crystal contraction, increasing the specific surface area and providing more active sites for lithium adsorption. The details for each type of doping technologies on LMO will be given on the following sections.

3.1.1. *Cations doping*

Qian et al. (2020a; 2021a) successfully doped monovalent metal ions K^+ and Na^+ into $Li_{1.6}Mn_{1.6}O_4$'s spinel structure without causing lattice distortion or creating impurity phases, maintaining the material's morphology. In this structure, Na^+ and K^+ mainly replace Li^+ at the 16d sites, either on the surface or in the bulk. Na^+ is more likely to replace surface Li^+ due to lower formation energy, while K^+ prefers bulk replacement. The enhancement of the stability of the spinel structure is mainly ascribed to the fact that:

(1) the replacement of Li at the 16d sites by Na or K has a negligible influence on the ion exchange effect between Li and H but can largely improve the stability of the spinel structure owing to the stronger Na-O and K-O bonds compared to that of Li-O bonds (Qian et al., 2020a; 2021a).
(2) the charge density of the 16d sites is gradually reduced with the Na and K doping, which is favorable to increasing the average valence state of Mn, thereby minimizing the disproportionated reaction of Mn^{3+} (Jahn–Teller effect) (Qian et al., 2020a; 2021a).

K-doped $Li_{1.6}Mn_{1.6}O_4$ shows an adsorption capacity of 26.0 mg g^{-1}, close to the undoped capacity (25.9 mg g^{-1}) and reduces Mn ion dissolution from 5.4% to 4.0% (Table 2). Na-doped $Li_{1.6}Mn_{1.6}O_4$ achieves a slightly higher adsorption capacity of 33.9 mg g^{-1} (0.4 mg g^{-1} higher than the undoped variant) and lowers Mn dissolution from 5% to 4.4%. After six cycles, K-doped $Li_{1.6}Mn_{1.6}O_4$ retains 90.8% of its adsorption capacity, outperforming Na-doped $Li_{1.6}Mn_{1.6}O_4$ with 87% (Table 2).

Doping multivalent ions like Mg^{2+}, Ga^{3+}, Zr^{4+}, Fe^{3+}, Al^{3+}, and Cr^{3+} in LMO primarily replaces Mn^{3+} ions, impacting the material differently than monovalent ion doping. Mg^{2+} (0.72 Å), Ga^{3+} (0.76 Å), and Zr^{4+} (0.79 Å) cations are the ones with radii slightly larger than Mn^{3+} (0.66 Å), the doped LMO are supposed to retain its original spinel structure, but with an expanded lattice constant and improved average valence of Mn (Bao et al., 2022; Wang et al., 2022; Ju et al., 2022). Al^{3+} (0.57 Å), Fe^{3+} (0.55 Å), and Cr^{3+} (0.62 Å) cations are the ones with radii slightly smaller than Mn^{3+}, the doping of such kind of cations can cause the crystal shrinkage and increase the specific surface area. Moreover, the partially replacement of Mn^{3+} by doped ions can create new bonds (Al-O, Fe-O, and Cr-O bonds) with stronger bond energy (Zhang et al., 2019; Gao et al., 2021; Cao et al., 2019).

In the case of Mg^{2+} (Bao et al., 2022), Ga^{3+}(Ju et al., 2022) and Zr^{4+} (Wang et al., 2022) doped LMO, the average valence of Mn showed separate increments from 3.58 to 3.72, 3.36 to 3.45, and 3.94 to 3.98. This increase in valence can mitigate the disproportionation reaction of Mn^{3+}, thus contributing to enhanced structural stability. However, Zr^{4+} doping may lead to the formation of a dense ZrO_2 layer above the LMO surface rather than lattice substitution. Following Mg^{2+} doping (Bao et al., 2022), the adsorption capacity witnessed a slight rise from 33.2 mg g^{-1} to 35.6 mg g^{-1}, maintaining 60% of its initial performance after 10 cycles . Correspondingly, the dissolution rate of Mn decreased from 3.23% to 0.55% (Table 2). On the other hand, for Ga^{3+} (Ju et al., 2022) and Zr^{4+} (Wang et al., 2022) doping, the adsorption capacity remained relatively lower, measuring 25.3 mg g^{-1} (undoped: 24.48 mg g^{-1}) and 25.96 mg g^{-1} (28.88 mg g^{-1}), respectively. Ga^{3+} doped LMO sustained 68.25% of its original performance after 8 cycles, while Zr^{4+} doped LMO continued to exhibit stable performance even after 15 cycles (sustained 92.18% of its original performance), with the Mn dissolution rate reduced from 0.349% to 0.293% (Table 2). The difference in adsorption capacity is closely related to factors such as the type of precursors, synthesis method, initial concentration of the adsorption solution, and pH conditions.

In the context of Al^{3+} (Qian et al., 2021b; Chen et al., 2018; Zhang et al., 2019), Fe^{3+} (Gao et al., 2021), and Cr^{3+} (Cao et al., 2019) doping, the enhancement of structural integrity can be attributed to the elevation of the average valence of Mn^{3+} and the introduction of stronger chemical bonds (Al-O, Fe-O, Cr-O) due to the partial substitution of Mn^{3+}. For instance, researchers such as Zhang et al. (2019) and Chen et al. (2018) separately incorporated Al into the spinel structure of LMO using $Li_{1.6}Mn_{1.6}O_4$ and $LiMn_2O_4$ as precursors. This led to an increase in the average valence of Mn from 3.58 to 3.65 and from 3.533 to 3.723, respectively. With Fe^{3+} doping (Gao et al., 2021), the valence value rose from 3.41 to 3.61. In the case of Al doping within the $Li_{1.6}Mn_{1.6}O_4$ structure (Zhang et al., 2019), the adsorption capacity elevated from 27.6 mg g^{-1} to 32.6 mg g^{-1}, retaining 82.2% of its initial performance

Table 2
Adsorption performance of different types of doped LMO.

Doped Element	LMO precursors	Dopant valence	Solution	AC, mg g^{-1}	Metals dissolution rate,%	Acid pickling	Recyclability	Ref.
K	$Li_{1.6}Mn_{1.6}O_4$	+1	0.5 g L^{-1} LiCl, pH=12	26.0	4.0	0.6 mol L^{-1} HCl	6 cycles, 90.8%	(Qian et al., 2020a)
Na	$Li_{1.6}Mn_{1.6}O_4$	+1	1.0 g L^{-1} LiCl, pH=12	33.9	4.4	0.6 mol L^{-1} HCl	6 cycles, 87%	(Qian et al., 2021a)
Mg	$Li_{1.6}Mn_{1.6}O_4$	+2	0.4 g L^{-1} LiCl, pH=12	35.6	3.23	0.5 mol L^{-1} HCl	10 cycles, 60%	(Bao et al., 2022)
Ga	$LiMn_2O_4$	+3	0.05 g L^{-1} LiCl, pH=9	25.3	4.65	0.1 mol L^{-1} HCl	8 cycles, 68.25%	(Ju et al., 2022)
Zr	$Li_{1.6}Mn_{1.6}O_4$	+4	Qinghai Kunty salt lake brine	25.96	0.349	0.1 mol L^{-1} HCl	15 cycles, 92.18%	(Wang et al., 2022)
Al	$LiMn_2O_4$	+3	0.05 g L^{-1} LiOH, pH=8–9	27.66	3.71	0.1 mol L^{-1} HCl	5 cycles, 74%	(Chen et al., 2018)
Al	$Li_{1.6}Mn_{1.6}O_4$	+3	1.0 g L^{-1} LiCl, pH=12	40.9	2.1	0.6 mol L^{-1} HCl	6 cycles, 94%	(Qian et al., 2021b)
Al	$Li_{1.6}Mn_{1.6}O_4$	+3	2.1 g L^{-1} LiOH, pH=12	32.6	1.92	0.5 mol L^{-1} HCl	4 cycles, 82.2%	(Zhang et al., 2019)
Fe	$LiMn_2O_4$	+3	0.05 g L^{-1} LiCl, pH=12	34.8	0.51%	1 mol L^{-1} HCl	5 cycles, 70%	(Gao et al., 2021)
Cr	$Li_{1.6}Mn_{1.6}O_4$	+3	salt lake brine	31.67	2.1	0.5 mol L^{-1} HCl	20 cycles, 21.7%	(Cao et al., 2019)
F, S	$Li_{1.6}Mn_{1.6}O_4$	-1, -2	0.5 g L^{-1} LiCl, pH=12	F: 33.4 S: 27.9	F: 5.4 S: 6.6	0.6 mol L^{-1} HCl	6 cycles, F: 86.52%, S: 85.66%	(Qian et al., 2020b)
F	$Li_{1.6}Mn_{1.6}O_4$	-1	0.35 g L^{-1}, pH=12	32.84	1.58	0.5 mol L^{-1} HCl	5 cycles, 91.29%	(Zhang et al., 2021)
Al-F	$Li_{1.6}Mn_{1.6}O_4$	+3, -1	0.35 g L^{-1}, pH=12	33.7	1.8	0.5 mol L^{-1} HCl	5 cycles, 92.13%	(Zhang et al., 2022)
Al-Fe	$Li_{1.6}Mn_{1.6}O_4$	+3, +3	0.1 g L^{-1}, pH=10.5	45.31	3	0.3 mol L^{-1} HCl	5 cycles, 95%	(Han et al., 2022)

Note: AC, adsorption capacity, mg/g means mg Li^+/ g active material.

and a Mn dissolution rate of 1.92% after 4 cycles (Table 2). Similarly, Al doped $LiMn_2O_4$ exhibited an adsorption capacity of 27.66 mg g^{-1} (undoped: 32.4 mg g^{-1}), maintaining 74% of its original performance, with a Mn dissolution rate of 3.71% after 5 cycles (Table 2). For Fe^{3+} (Gao et al., 2021) and Cr^{3+} (Cao et al., 2019) doped LMO, the adsorption capacities measured 34.8 mg g^{-1} (undoped: 38.6 mg g^{-1}) and 31.67 mg g^{-1} (undoped: 30.8 mg g^{-1}), respectively. Following 5 and 20 cycles, they retained 70% and 81.7% of their initial performance, respectively. Notably, Fe^{3+} doping led to a reduction in the Mn dissolution rate from 2.48% to 0.51%, while the Mn dissolution rate for Cr^{3+} doped LMO stood at 2.1% (Table 2).

In the case of Al^{3+} doped $Li_{1.6}Mn_{1.6}O_4$ synthesized by Qian et al. (2021b), it was revealed that, apart from lattice substitution, the doped Al primarily localized in the surface layer and did not permeate the crystal lattice's bulk. The surface exhibited a lower formation energy than the bulk, reaching its minimum at the 16d sites on the surface (0.67 eV), confirming the presence of Al doping at the surface layer (Fig. 6a-d). Moreover, the Mn atoms in proximity to the Al atoms experienced a greater charge loss compared to those farther from the Al atoms, indicating an elevation in the average valence of Mn due to Al doping (Fig. 6e-f). This enhancement contributed to an improved resistance against dissolution. Notably, the adsorption capacity escalated from 33.4 mg g^{-1} to 40.9 mg g^{-1}, and even after 6 cycles, it retained 94% of its original performance, with the Mn dissolution rate remaining below 2.1% (Table 2) (Qian et al., 2021b).

The above research results indicate that cation doping in LISs can effectively enhance their stability. This enhancement is primarily achieved by substituting some of the trivalent manganese in the structure of the LISs, thereby providing stronger chemical bonds and reducing the content of trivalent manganese (Qian et al., 2021b; Chen et al., 2018; Zhang et al., 2019; Gao et al., 2021; Cao et al., 2019). Such substitutions alter the overall valence state of the structure, leading to a decrease in manganese dissolution (Zhang et al., 2019). It is noteworthy, however, that despite the improved structural stability of the LISs, their adsorption performance does not necessarily enhance and may even decrease. This is mainly because the substitution of metal ions reduces the number of active sites available for Li-H exchange, consequently diminishing the adsorption capacity. Balancing the relationship between structural stability and adsorption performance requires further study. Additionally, research is needed to determine whether the doped metal ions also exhibit solubility behavior and whether they produce environmentally harmful substances.

3.1.2. *Anions doping*

Qian et al. (2020b) and Zhang et al. (2021) both explored anionic doping in the spinel structure of $Li_{1.6}Mn_{1.6}O_4$, focusing on fluorine (F^-) and sulfur (S^{2-}) ions. They found that doping with F^- and S^{2-} had minimal impact on the particle morphology of $Li_{1.6}Mn_{1.6}O_4$. F^- ions, due to their smaller size compared to S^{2-}, were more readily incorporated into the lattice. F^- doped $Li_{1.6}Mn_{1.6}O_4$ showed a higher adsorption capacity than S-doped and undoped samples, with Density Functional Theory (DFT) calculations suggesting that F^- or S^{2-} doping most likely replaces O at 32e sites in the bulk, improving charge density and adsorption-desorption efficiency (Fig. 7).

Zhang et al.'s approach (Zhang et al., 2021), however, revealed that direct doping of fluorine on $Li_{1.6}Mn_{1.6}O_4$ is akin to surface fluorination, with fluorine atoms mostly residing on the material's surface rather than within the bulk. This surface fluorination changes the material's microstructure but not its underlying spinel structure. The process slightly lowers the average Mn valence, indicating a partial replacement of O^{2-} by $F^-$and the reduction of Mn^{4+} to Mn^{3+}. Surface fluorination also leads to a stronger bond energy between F 2p and Mn 3d orbitals than between O 2p and Mn 3d orbitals, enhancing structural stability and increasing charge density at the doping site.

Surface fluorination (Zhang et al., 2021) and lattice fluorination (Qian et al., 2020b) yield different adsorption results. Surface fluorination (Zhang et al., 2021) slightly changes the adsorption capacity, with the fluorinated sample showing a capacity of 32.84 mg g^{-1} (undoped: 31.59 mg g^{-1}) for Li^+ and retaining 91.29% of this capacity over five cycles, along with a reduced Mn dissolution rate (1.58%) (Table 2). In contrast, lattice fluorination with F^- and S^{2-} leads to higher Li^+ adsorption capacities (33.4 mg g^{-1} and 27.9 mg g^{-1}, respectively) compared to unmodified LMO (26.1 mg g^{-1}) (Table 2) (Qian et al., 2020b). These doped materials maintain substantial portions of their initial capacities over six cycles, but with higher Mn dissolution rates. Surface fluorination's effectiveness in reducing Mn dissolution is attributed to the formation of a protective LiF layer, while lattice fluorination likely improves adsorption through increased charge density.

Anion doping primarily involves surface doping and lattice doping. Compared to surface doping, lattice doping can more effectively enhance the adsorption performance of LISs. Moreover, selecting anions with a radius similar to oxygen for doping can relatively maintain structural stability and improve adsorption performance (Qian et al., 2020b; Zhang et al., 2021). However, unlike cation doping, anion doping does not significantly enhance the structural stability. In fact, it may even exacerbate the dissolution of manganese ions compared to the undoped structure. Additionally, fluoride and sulfide ions are environmentally harmful. If these ions are also released from the structure, it could lead to secondary pollution.

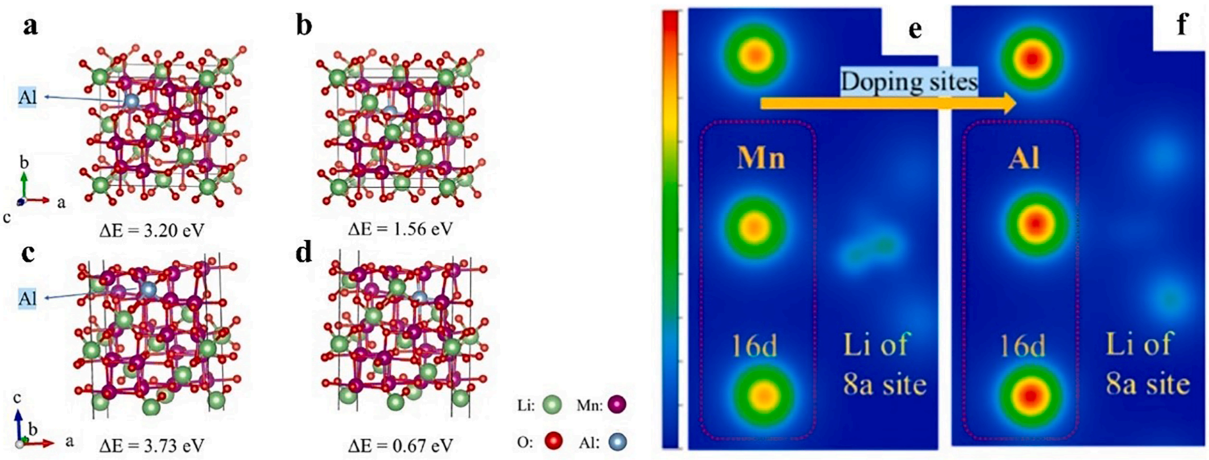

Fig. 6. Optimized structures of replacing Li or Mn sites with Al: (a) 8a, (b) 16d site in bulk; (c) 8a, (d) 16d site in surface; The charge density contour of LMO of (e) bare and (f) Al gradient doping (Qian et al., 2021b).

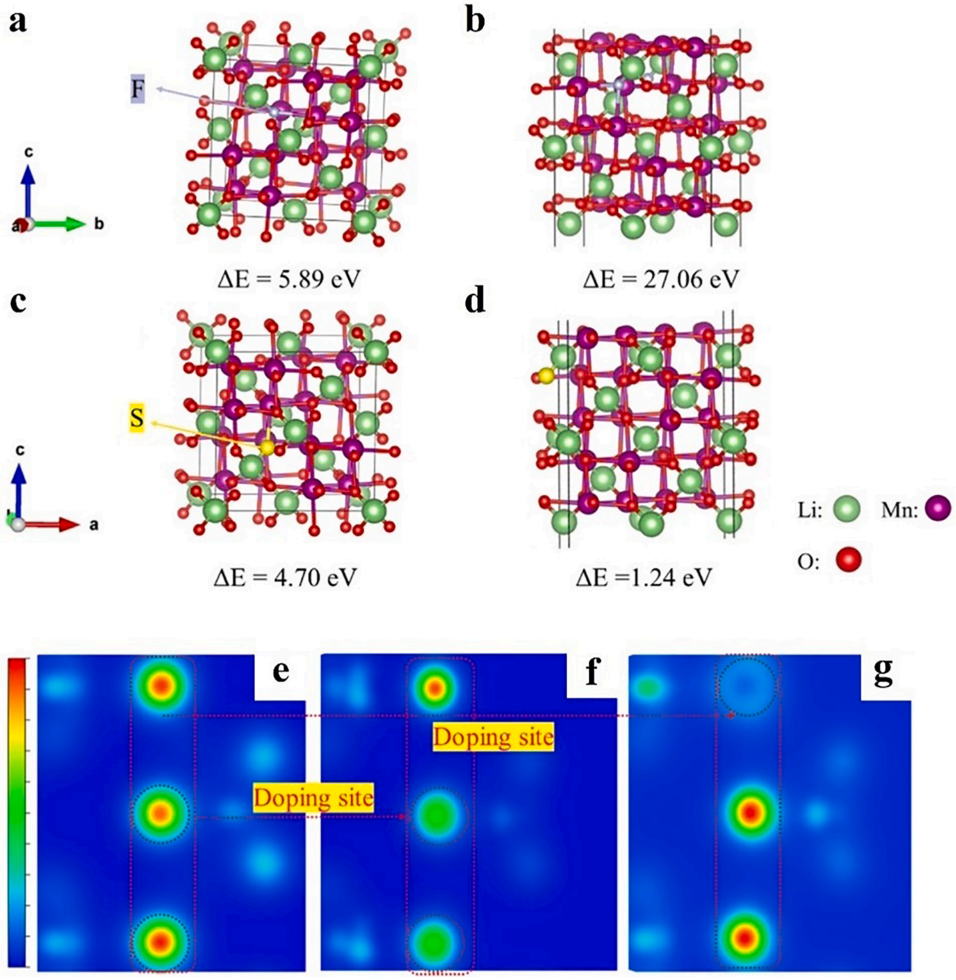

Fig. 7. Optimized structures with substitution of O by F or S anions. (a) Li at 8a sites and (b) Li at 16d sites in bulk. (c) Li at 8a sites and (d) Li at 16d sites on the (100) surface; The charge density maps for the (e) undoped LMO; (1 0 0) surface of LMO with (f) F-doping and (g) S doping at the 32e sites (Qian et al., 2020b).

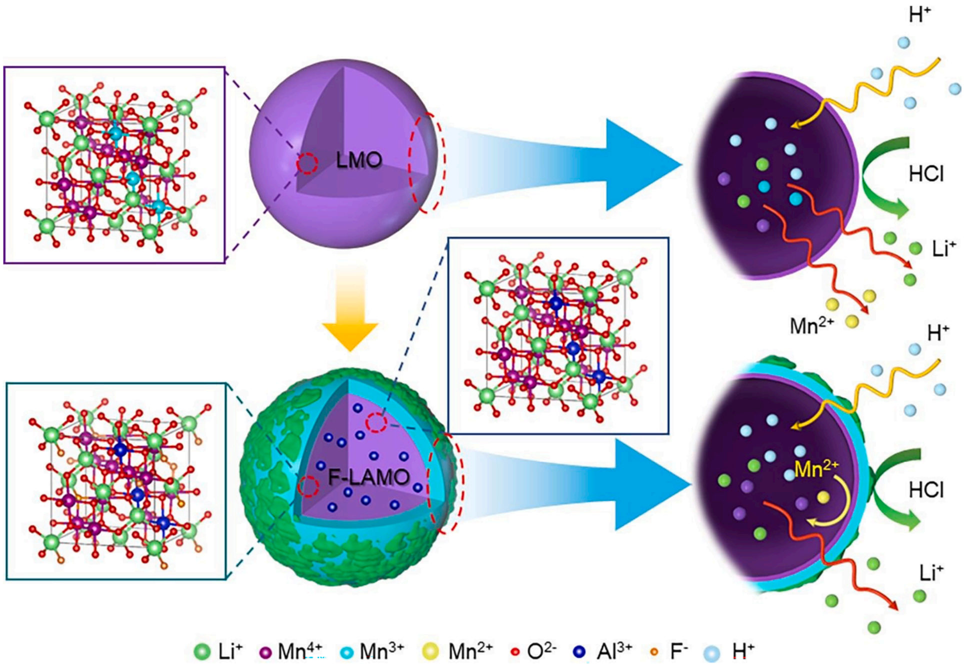

Fig. 8. Schematic of the proposed structural model and action mechanism of the synthesized materials (Zhang et al., 2022).

3.1.3. Co-doping

The aforementioned results indicates that anionic doping of LMO improves adsorption capacity, while cationic doping enhances structural stability. A synergistic effect is hypothesized for co-doping with anions and cations.

Zhang et al. (2022) utilized a co-doping strategy that incorporated both Al and F ions into the spinel structure of $Li_{1.6}Mn_{1.6}O_4$. The experimental outcomes underscore that the co-doping of Al and F induces lattice contraction while minimally affecting the overall shape of the adsorbent. However, the particle dimensions exhibit a significant reduction, accompanied by the development of a roughened surface. Intriguingly, fine nanoparticles (referred to as nano-islands) appear on the F-LAMO surface, potentially contributing to a substantial enhancement in the diffusion kinetics of Li^+ within the adsorbent. This improvement can be attributed to the presence of abundant active sites and a larger surface area (Fig. 8). The origin of these surface nano-islands may lie in the etching of the bulk LMO surface during NH_4F modification. Furthermore, F doping is more prone to form an AlF_3 coating layer atop the $Li_{1.6}Mn_{1.6}O_4$ surface, safeguarding the structural integrity against degradation. In contrast, Al^{3+} metal ions possess the capacity to partially replace Mn^{3+} within the crystal lattice bulk, leading to uniform distribution. The augmented structural stability and adsorption capacity are grounded in the following factors: (1) The bond lengths of formed Mn-F and Al-O bonds are 1.80 Å and 2.11 Å, respectively, shorter than that of Mn-O (2.24 Å). This reduction in bond length translates to increased bond energy and heightened stability; (2) The creation of an AlF_3 coating layer, acting as a robust ion conductor, fosters the diffusion of Li^+. Simultaneously, the emergence of nano-islands on the surface fosters roughening and augments the specific surface area for Li^+ interaction. This cumulative effect significantly amplifies the adsorption capacity. The co-doped Al-F LMO manifests a significant enhancement in Li^+ adsorption capacity compared to the undoped counterpart (rising from 28.5 to 33.7 mg g^{-1}). Remarkably, even after undergoing five cycles, it retains an impressive 92.13% of its initial lithium capacity and demonstrates a minimal Mn dissolution rate of just 1.62%, thereby establishing its good cycling stability (Table 2).

In addition to the incorporation of cations and anions, the simultaneous integration of dual cations emerges as a promising co-doping strategy (Han et al., 2022). Considering that the ionic radii of Al^{3+} (0.57 Å) and Fe^{3+} (0.55 Å) are smaller than that of Mn^{3+} (0.66 Å), co-doping both these cations into the spinel structure of LMO could potentially induce grain contraction (Han et al., 2022). Nevertheless, this shrinkage could be counterbalanced by the formation of robust Al-O and Fe-O bonds, thereby compensating for the reduced structural stability. Importantly, the introduction of dually integrated cations also imparts magnetic properties to the doped LMO, a beneficial outcome stemming from the partial substitution of Mn^{3+} with Fe^{3+}. This enhanced magnetism not only augments the material's overall functionality but also holds the potential to enhance its viability for subsequent recycling applications. The co-doped LMO displayed a significantly higher lithium adsorption capacity than undoped LMO (rising from 29.44 mg g^{-1} to 45.31 mg g^{-1}), maintaining a high capacity over five cycles with low Mn dissolution rates (retains an impressive 95% of its initial lithium capacity after five cycles and demonstrates a minimal Mn dissolution rate of 3%) (Table 2) (Han et al., 2022).

The strategy of co-doping in LISs, encompassing both anion-cation and cation-cation co-doping modalities, is instrumental in concurrently augmenting the adsorption efficacy and the structural robustness of the LISs. Notably, cation-cation co-doping exhibits a marked superiority over anion-cation co-doping in terms of substantially enhancing lithium adsorption capacity, while also maintaining commendable recyclability. Consequently, it is imperative for forthcoming research to delve more deeply into the prospects of cation-cation co-doping. Furthermore, empirical testing of these co-doped and modified adsorbents in real brine solutions is recommended to rigorously assess their practical treatment efficiencies and applicability in real-world conditions.

3.2. Doping-modified advanced LTO for Li^+ adsorption

LTO is typically synthesized via a high-temperature solid-state reaction. However, this process often incurs aggregation due to high temperatures, subsequently affecting its practical applications (Wei et al., 2020). Ion doping serves to mitigate this aggregation phenomenon during synthesis, thereby enhancing its performance. Simultaneously, specific ions can impart unique functionalities to the modified material. For instance, Fe doping endows LTO with magnetism, facilitating the recycling of the doped LTO. Furthermore, the introduction of Al^{3+}, with its stronger electronegativity compared to Ti^{4+}, can boost the adsorption of Li^+ by the doped LTO, thereby augmenting its efficiency.

Enhancing the properties of LTO through doping with various elements has been well studied. Wang et al. incorporated Fe (Wang et al., 2018a; 2018b) and Mo (Wang et al., 2019) into LTO, using synthetic solutions and practical brines to test the material's stability and selectivity. The authors indicated that Fe doping not only conferred magnetic properties to LTO but also effectively reduced particle aggregation, thus aiding in recycling and reuse. On the other hand, Zhou et al. (2022) doped Zr into LTO using a solid-state reaction method. This approach yielded a more homogeneous product and decreased grain size, which helped to reduce particle aggregation. The increase in surface area and pore volume as a result of this grain size reduction significantly enhanced the adsorption performance of the material. Additionally, doping with Mo and Zr was found to increase the oxygen content in LTO from 53.26% to 61.58% and 54.96% to 70.13%, respectively. This higher oxygen content provided additional active sites for lithium adsorption, thereby boosting the overall efficacy of the LTO.

Dai et al. (2021) conducted a study on doping LTO with Al^{3+} ions, focusing on improving the material's properties for lithium adsorption. The research showed that Li-Al layered double hydroxide, which has a strong affinity for Li^+ ions, benefits from the higher electronegativity of Al^{3+} compared to Ti^{4+} ions. This results in a stronger attraction to positively charged ions like Li^+. The primary objectives of doping Al^{3+} into the layered Li_2TiO_3 structure were to reduce particle aggregation during the calcination process and to enhance the selective adsorption of Li^+ ions. In contrast to doping with Fe, Mo, and Zr ions, Al doping did not significantly alter the crystal structure of LTO, nor did it cause the grains of the doped product to shrink or expand. This indicates that Al^{3+} doping effectively maintains the structural integrity of LTO, preserving its original beneficial properties while also improving its capacity for Li^+ ion adsorption.

Post-doping modifications significantly influence the lithium adsorption performance of LTO. For Fe-doped LTO (Wang et al., 2018a), treating a synthetic solution with a lithium hydroxide concentration of 1.8 g L^{-1} at pH 12, the adsorption capacity slightly increased from 50.5 mg g^{-1} to 53.3 mg g^{-1}, with Ti loss maintained at $\leq$1% and Fe loss stabilizing around 1.5% over multiple cycles (Table 3). However, in practical brine with a pH of 8.8, the maximum adsorption capacity dropped to 34.8 mg g^{-1} due to enhanced ion exchange (Wang et al., 2018b). Despite this, the stability and adaptability of Fe-doped LTO remained robust. Its magnetic properties, introduced by Fe doping, improved recyclability, allowing for 90% solid powder recycling in 15 mins using flowing N_2 gas. In contrast, Mo (Wang et al., 2019) and Zr (Zhou et al., 2022) doping significantly raised the adsorption capacity of LTO to 78 mg g^{-1} and 93.2 mg g^{-1}, respectively, primarily due to increased O^{2-} content in the structure. Zr-doped LTO was also transformed into a granular form, slightly reducing its capacity to 47.5 mg g^{-1} but maintaining good recycling performance and a Ti dissolution rate under 2% (Table 3). Al-doped LTO showed a modest increase in adsorption capacity to 32.12 mg g^{-1}, preserving 91.3% of its efficacy over five cycles with a Ti dissolution rate of 1.7% (Table 3) (Dai et al., 2021).

In summary, by doping layered LTO with metal ions, the particle

Table 3
Adsorption performance of different types of doped LTO.

Doped element	LTO precursors	Dopant valence	Solution	AC, mg g^{-1}	Metals dissolution rate,%	Acid pickling	Recyclability	Ref.
Fe	Li_2TiO_3	+3	1.8 g L^{-1} LiOH, pH = 12	53.3	Ti: ≤1%; Fe: ~1.5%	0.5 mol L^{-1} HCl	10 cycles, >95%	(Wang et al., 2018a)
Fe	Li_2TiO_3	+3	1.56 g L^{-1}, Brine, pH = 8.8	34.8	Ti: ≤1%; Fe: ~1.5%	0.5 mol L^{-1} HCl	9 cycles, >95%	(Wang et al., 2018b)
Mo	Li_2TiO_3	+4	1.8 g L^{-1} LiOH, pH = 12	78	–	0.5 mol L^{-1} HCl	6 cycles, >95%	(Wang et al., 2019)
Al	Li_2TiO_3	+3	1.5 g L^{-1} LiCl, pH = 12	32.12	Ti: 1.7%;	0.6 mol L^{-1} HCl	5 cycles, 91.2%	(Dai et al., 2021)
Zr	Li_2TiO_3	+4	1.8 g L^{-1} LiOH, pH = 12	93.2	Ti: ≤2%;	0.25 mol L^{-1} HCl	5 cycles, ~99%	(Zhou et al., 2022)

Note: AC, adsorption capacity, mg/g means mg Li^+/ g active material.

aggregation caused by high-temperature solid-state reactions can be effectively alleviated. Appropriate doping can reduce the grain size, which not only mitigates particle aggregation but also increases the specific surface area and pore volume, providing more active sites for lithium adsorption. Different metal ion dopants can endow LTO with specific functionalities. For instance, iron doping imparts certain magnetic properties to the modified LTO, facilitating its subsequent cyclic recovery and reuse. However, during the doping process of LTO, considerations should also be given to the economic costs of the dopant ions and their leaching behavior post-doping.

4. Li^+ ions adsorption kinetics and adsorption isotherms over heteroatom doped LISs

Equilibrium isotherm modeling and kinetics modeling are critical tools in interpreting adsorption data, crucial for understanding the efficiency, sorbent utilization, and key parameters essential for scaling up the adsorption process. Adsorption kinetic models, including the pseudo first-order, pseudo-second order, intraparticle diffusion, and film diffusion models, are instrumental in evaluating the efficiency and rate-determining steps of Li^+ adsorption onto LISs (Limjuco et al., 2016; Gu et al., 2018; Sun et al., 2023). These models help to elucidate the overall adsorption mechanism and identify the rate-limiting steps. The pseudo-first-order model, indicative of physical diffusion in solid-liquid systems, and the pseudo-second-order model, suggestive of chemisorption, are particularly significant. According to Table 4, it can be concluded that the pseudo-second-order model is often found to better represent Li^+ adsorption kinetics on LISs than the pseudo-first-order model. Furthermore, the majority of the modified LISs discussed require a minimum of 24 h to complete the adsorption process. This duration indicates a relatively slow adsorption rate, underscoring the need for further enhancements to improve the efficiency of the process. Adsorption isotherms, such as the Langmuir and Freundlich models, describe the equilibrium performance of adsorbents at constant temperatures, dependent on various factors like pH, ionic strength, and the nature of the adsorbate and adsorbent. The Langmuir model assumes uniform adsorbent surfaces and monolayer adsorption, while the Freundlich model is suited for non-uniform surfaces and can describe both monolayer and multilayer adsorption scenarios (Gu et al., 2018; Shi et al., 2013; Yu and Sasaki, 2016; Han et al., 2018). Often, the Langmuir model more effectively characterizes Li^+ adsorption on LISs and doped LISs compared to the Freundlich model (Table 4).

However, research often lacks comparative studies of adsorption behavior before and after modification, which is crucial as the same adsorption model can yield different results based on varying parameters. Key parameters like the Langmuir model's separation coefficient (k_1) and the Freundlich model's adsorption coefficient (k_f) and 1/n factor play significant roles in depicting adsorption behavior and intensity. These variations highlight the need for a comprehensive assessment of how modifications impact adsorption dynamics, emphasizing the importance of detailed investigation in this field.

Table 4
Adsorption behavior of different types of heteroatom doped LISs.

Heteroatom doped LISs	Adsorption time, h	Adsorption behavior	Ref
K-LMO	48	Pseudo-second-order; Langmuir	(Qian et al., 2020a)
Na-LMO	48	Pseudo-second-order; Langmuir	(Qian et al., 2021a)
Mg-LMO	24	Pseudo-second-order; Langmuir	(Bao et al., 2022)
Ga-LMO	24	Pseudo-second-order; Langmuir	(Ju et al., 2022)
Zr-LMO	12	Pseudo-second-order; Freundlich isotherm	(Wang et al., 2022)
Al-LMO	48	Pseudo-second-order; Langmuir	(Qian et al., 2021b)
Al-LMO	24	Pseudo-second-order	(Zhang et al., 2019)
Fe-LMO	24	Pseudo-second-order; Langmuir	(Gao et al., 2021)
Cr-LMO	25	Pseudo-second-order	(Cao et al., 2019)
F, S-LMO	48	Pseudo-second-order; Langmuir	(Qian et al., 2020b)
F-LMO	24	Pseudo-second-order; Langmuir	(Zhang et al., 2021)
Al, F-LMO	24	Pseudo-second-order; Langmuir	(Zhang et al., 2022)
Al, Fe-LMO	24	Pseudo-second-order; Langmuir	(Han et al., 2022)
Fe-LTO	50	Pseudo-second-order; Langmuir	(Wang et al., 2018a)
Fe-LTO	50	Pseudo-second-order; Langmuir	(Wang et al., 2018b)
Mo-LTO	50	Pseudo-second-order; Langmuir	(Wang et al., 2019)
Al-LTO	8	Pseudo-second-order; Langmuir	(Dai et al., 2021)
Zr-LTO	24	Pseudo-second-order; Langmuir	(Zhou et al., 2022)

5. Practical applications of heteroatom doped LISs for Li^+ ions adsorption

The practical application of various ions doped LISs in actual solutions is crucial for their large-scale promotion. Table 5 presents the adsorption results of heteroatom doped LISs that are currently used in actual solutions. The compositions of the traditional coexisting ions like Na^+, K^+, Li^+, Mg^{2+} and Ca^{2+} and their corresponding adsorption capacity are given to demonstrate the feasibility and selectivity of heteroatom doped LISs for Li^+ adsorption.

As indicated by Table 5, heteroatom-doped LTO demonstrate superior adsorption performance in practical applications compared to

Table 5
Adsorption performance of different types of ions doped LISs for practical applications.

Types of LISs	Water resources	Ions concentration, mg L^{-1}	Mg/Li ratio	Adsorption performance, mg g^{-1}	Ref
K-LMO	Lagoco salt lake brine	Li^+: 253.5 Mg^{2+}: 787.5 K^+: 2439 Na^+: 16,726.9 Ca^{2+}: 38.36	0.88	Li^+: 18.39 Mg^{2+}: 0.19 K^+: 4.68 Na^+:47.38 Ca^{2+}: 0.04	(Qian et al., 2020a)
Na-LMO	Lagoco salt lake brine	Li^+: 261.5 Mg^{2+}: 802.1 K^+: 2432.0 Na^+:15,600 Ca^{2+}: 21.56	0.88	Li^+: 18.8 Mg^{2+}: 0.38 K^+: 9.36 Na^+:4.9 Ca^{2+}: 0.08	(Qian et al., 2021a)
Mg-LMO	Salt lake brine	Li^+: 156.0 Mg^{2+}: 301 K^+: 2310 Na^+: 39,000 Ca^{2+}: 4.00	1.93	Li^+: 35.0 Mg^{2+}: 0.44 K^+: 1.07 Na^+:3.42 Ca^{2+}: 0.09	(Bao et al., 2022)
Zr-LMO	Qinghai Kunty salt lake brine	Li^+: 154.95 Mg^{2+}: 10,523.69 K^+: 3630.06 Na^+: 5390.33 Ca^{2+}: 72.00	67.92	Li^+: 25.96 Mg^{2+}: 71.87 K^+: 0.07 Na^+:1.10 Ca^{2+}: 0	(Wang et al., 2022)
Fe-LMO	Synthetic salt lake brine	Li^+: 38.06 Mg^{2+}: 573.21 K^+: 150.36 Na^+: 1198.33 Ca^{2+}: 147.03	15.06	Li^+: 9.63 Mg^{2+}: 8.47 K^+: 0.78 Na^+:4.72 Ca^{2+}: 1.93	(Gao et al., 2021)
F-LMO	Qarhan brine.	Li^+: 92.45 Mg^{2+}: 65,008 K^+: 13,408 Na^+: 15,023 Ca^{2+}: 10,708	703.17	Li^+: 15.36 Mg^{2+}: 0 K^+: 1.89 Na^+:0 Ca^{2+}: 0.08	(Zhang et al., 2021)
Al-F-LMO	Qarhan brine	Li^+: 72.7 Mg^{2+}: 67,621 K^+: 13,711 Na^+: 16,753 Ca^{2+}: 10,559	930.14	Li^+: 16.44 Mg^{2+}: 0.91 K^+: 2.21 Na^+:0.80 Ca^{2+}: 2.11	(Zhang et al., 2022)
Fe-LTO	Concentrated Brine	Li^+: 1510 Mg^{2+}: 52,600 K^+: 540 Na^+: 1630 Ca^{2+}: 56,800	34.83	Li^+: 34.7 Mg^{2+}: 2.11 K^+: 0.82 Na^+:0.96 Ca^{2+}: 1.64	(Wang et al., 2018a)
Fe-LTO	Brine	Li^+: 1560 Mg^{2+}: 55,200 K^+: 500 Na^+: 1600 Ca^{2+}: 58,500	35.38	Li^+: 34.8 Mg^{2+}: 2.26 K^+: 1.29 Na^+:1.13 Ca^{2+}: 1.67	(Wang et al., 2018b)
Mo-LTO	Brine	Li^+: 1510 Mg^{2+}: 52,600 K^+: 540 Na^+: 1630 Ca^{2+}: 56,800	34.83	Li^+: 39.5 Mg^{2+}: 1.69 K^+: 0.67 Na^+:0.89 Ca^{2+}: 1.44	(Wang et al., 2019)
Zr-LTO	Simulated salt lake brine	Li^+: 1560 Mg^{2+}: 55,200 K^+: 760 Na^+: 1600 Ca^{2+}: 56,800	35.38	Li^+: 51.8 Mg^{2+}: 1.86 K^+: 0.3 Na^+:0.95 Ca^{2+}: 1.64	(Zhou et al., 2022)

heteroatom-doped LMO. For instance, LMO doped with monovalent heteroatoms (e.g., K^+ (Qian et al., 2020a) and Na^+(Qian et al., 2021a)) exhibit an adsorption capacity of only 18 mg g^{-1} for Li^+ in salt lake brines. They also show some adsorption affinity for $K^+$and Na^+ ions, likely due to the ion doping imparting a certain ion memory effect for these ions. In contrast, LMO doped with multivalent ions like Mg^{2+} (Bao et al., 2022), Zr^{4+} (Wang et al., 2022), and Fe^{3+} (Gao et al., 2021) only show better selectivity for lithium in scenarios where the Mg^{2+}/Li^+ ratio is low (e.g., 1.93). However, when the concentration of Mg^{2+} ions in the brine is high (e.g., Mg^{2+}/Li^+: 67.92 and 15.06), these sieves also exhibit adsorption for Mg^{2+}, indicating poorer selectivity. In comparison, LTO doped with heteroatoms (Wang et al., 2018a; Wang et al., 2018b; Wang et al., 2019; Zhou et al., 2022), in conditions where the Mg^{2+}/Li^+ ratio is 35, and with K^+ and Na^+ concentrations around 500 mg L^{-1} and 1600 mg L^{-1} respectively, show Li^+ adsorption capacities exceeding 34 mg g^{-1}. Moreover, their adsorption for other ions remains below 3 mg g^{-1}, demonstrating exceptional selectivity and adsorptive capacity. In practical applications, heteroatom-doped LTO present a more promising outlook compared to heteroatom-doped LMO.

Notably, when LMO undergo anion doping and co-doping, they exhibit good Li^+ adsorption even under very high Mg^{2+}/Li^+ ratio (e.g., 703.17 (Zhang et al., 2021), and 930.14 (Zhang et al., 2022)), while maintaining low adsorption for Mg^{2+} (below 1 mg g^{-1}). Additionally, in conditions with high Na^+ and K^+ concentrations (over 13,000 mg L^{-1}), their adsorption for these ions remains below 3 mg g^{-1}, indicating exceptional selectivity. However, their adsorption capacity for Li^+ is lower compared to LTO doped with heteroatoms, likely due to the lower initial concentration of Li^+ ions in the solution.

In conclusion, LMO with anion doping and co-doping, as well as heteroatom-doped LTO, exhibit significant promise for applications in salt lake brines. Particularly, the heteroatom-doped LTO demonstrate excellent cyclic performance in single-solution adsorption processes.

6. Conclusions and future outlooks

6.1. Conclusions

This review highlights the role of heteroatom doped LISs in enhancing lithium recovery from brines, key to optimizing water resources and meeting the growing lithium demand. LISs, primarily LMO and LTO, show high lithium selectivity despite coexisting ions like K^+, Ca^{2+}, Na^+, and Mg^{2+}. Challenges include Mn^{3+} or Ti^{4+} ion dissolution affecting stability and particle aggregation during synthesis. Heteroatom doping, including cationic, anionic, and co-doping, improves these issues by stabilizing the valence state in LMO and reducing aggregation in LTO. Doping can occur on the surface or within the lattice, depending on the synthesis stage and dopant properties. These enhancements in doped LISs lead to better stability, selectivity against interfering ions, and prolonged reuse cycles, presenting a promising advancement in efficient lithium extraction from brines.

6.2. Future outlooks

Despite encouraging strides, the field of Li^+ ion adsorption using ions doped LISs is still relatively nascent. The challenges and future perspectives are outlined as follows:

Firstly, the modification methods are time-consuming, with some even requiring up to 48 h to complete the synthesis process. Furthermore, these procedures can be quite intricate in nature. Comparisons between modified and unmodified LISs adsorbents are often lacking, failing to effectively showcase the advantages of the modification processes. Another limitation of LISs adsorbents lies in their extended adsorption times and suboptimal adsorption capacities. Satisfactory adsorption outcomes tend to manifest only when higher Li^+ ion concentrations present. Unfortunately, heteroatom doping does not seem to notably enhance this aspect of adsorption performance. This highlights the need for further research and innovation to address these challenges and enhance the efficiency of LISs-based adsorption systems.

Secondly, the practical application of LISs adsorbents remains largely confined to laboratory scales. While LISs demonstrate promising adsorption performance in comparison to other adsorbents, their utilization on an industrial scale remains limited. Future research efforts should shift towards treating real-world solutions, with the aim of developing adsorbents that exhibit heightened selectivity. Modification endeavors should prioritize the integration of lower-cost ions. This would ensure that the adsorbents can effectively withstand the influence of coexisting ions, enabling selective adsorption of Li^+ ions even in solutions characterized by high Mg^{2+}/Li^+ ratios. In parallel, it is essential to conduct continuous adsorption experiments utilizing specialized devices such as adsorption columns. This approach mimics the actual adsorption and desorption processes, furnishing valuable data to support subsequent industrial implementation. This shift towards practical application and refinement is crucial to realizing the full potential of LISs adsorbents in addressing the growing demand for lithium resources.

Thirdly, the mechanism of doping modification is indeed not clearly described in many current reports. Most studies attribute this modification to lattice doping, but the reality might be more complex. The doping mechanism and effect of heteroatoms are indeed influenced by various factors. The most crucial factor is the inherent chemical properties of the ions themselves. For example, some ions might more easily embed into the lattice due to their radius and charge state matching well with the host lattice. In contrast, other ions might prefer to form doping or simple coverage on the lattice surface due to a mismatch with the lattice. To delve deeper into the doping mechanism, the following methods and techniques might be extremely useful: high-resolution transmission electron microscopy (HRTEM), X-ray Photoelectron Spectroscopy (XPS), DFT calculations, and Raman Spectroscopy and Infrared Spectroscopy.

Finally, emphasis should be placed on both the structural stability and potential environmental risks posed by adsorbents. The degradation of adsorbents could result in the leaching of cations and anions and the generation of nano-sized particles. The release of these byproducts into water bodies has the potential to trigger secondary pollution. Moreover, interactions between adsorbents and other species in water may give rise to the formation of novel contaminants. These adverse aspects bear significant relevance to the practical applications of adsorbents. Consequently, a critical need arises to evaluate the stability of adsorbents in real-world water systems. Furthermore, the efficient and complete removal of adsorbents from water following their utilization presents an additional challenge. Addressing these concerns is vital to ensuring the responsible deployment of adsorbents for Li^+ recovery purposes.

CRediT authorship contribution statement

Qian Chen: Methodology, Data curation, Investigation, Formal analysis, Writing – original draft, Writing – review & editing. **Zhijie Chen:** Conceptualization, Methodology, Formal analysis, Supervision, Validation, Writing – review & editing. **Hongqiang Li:** Formal analysis, Validation, Writing – review & editing. **Bing-Jie Ni:** Conceptualization, Supervision, Writing – review & editing, Funding acquisition.

Declaration of competing interest

The authors declare that they have no known competing financial interests or personal relationships that could have appeared to influence the work reported in this paper.

References

Aljarrah, S., Alsabbagh, A., Almahasneh, M., 2023. Selective recovery of lithium from Dead Sea end brines using UBK10 ion exchange resin. Can. J. Chem. Eng. 101 (3), 1185–1194. https://doi.org/10.1002/cjce.24559, 2023/03/01.

Bao, L., Zhang, J., Wu, J., Zhang, G., Yang, Y., Tang, W., Xue, M., 2022. Preparation of Mg-doped $Li_{1.6}Mn_{1.6}O_4$ with enhanced Li^+ adsorption performance and anti-dissolution properties of Mn. Hydrometallurgy 209, 105772. https://doi.org/10.1016/j.hydromet.2021.105772, 2022/03/01/.

Cao, G., Yang, X., Yin, Z., Lei, Y., Wang, H., Li, J., 2019. Synthesis, Adsorption Properties and Stability of Cr-Doped Lithium Ion Sieve in Salt Lake Brine. Bull. Chem. Soc. Jpn. 92 (7), 1205–1210. https://doi.org/10.1246/bcsj.20190061.

Chen, M., Wu, R., Ju, S., Zhang, X., Xue, F., Xing, W., 2018. Improved performance of Al-doped $LiMn_2O_4$ ion-sieves for Li^+ adsorption. Micropor. Mesopor. Mater. 261, 29–34. https://doi.org/10.1016/j.micromeso.2017.10.058, 2018/05/01/.

Dai, X., Zhan, H., Qian, Z., Li, J., Liu, Z., Wu, Z., Oct 25 2021. Al-doped H_2TiO_3 ion sieve with enhanced Li^+ adsorption performance. RSC. Adv. 11 (55), 34988–34995. https://doi.org/10.1039/d1ra06535a.

European Commission, Directorate-General for Internal Market, Industry, Entrepreneurship and SMEs, Grohol, M., Veeh, C. (2023). Study on the critical raw materials for the EU 2023 : Final report, Publications Office of the European Union. https://data.europa.eu/doi/10.2873/725585.

Foo, Z.H., Thomas, J.B., Heath, S.M., Garcia, J.A., Lienhard, J.H., 2023. Sustainable Lithium Recovery from Hypersaline Salt-Lakes by Selective Electrodialysis: transport and Thermodynamics. Environ. Sci. Technol. 57 (39), 14747–14759. https://doi.org/10.1021/acs.est.3c04472, 2023/10/03.

Gao, J.-m., Du, Z., Zhao, Q., Guo, Y., Cheng, F., 2021. Enhanced Li^+ adsorption by magnetically recyclable iron-doped lithium manganese oxide ion-sieve: synthesis, characterization, adsorption kinetics and isotherm. J. Mater. Res. Technol. 13, 228–240. https://doi.org/10.1016/j.jmrt.2021.04.073, 2021/07/01/.

Gu, D., Sun, W., Han, G., Cui, Q., Wang, H., 2018. Lithium ion sieve synthesized via an improved solid state method and adsorption performance for West Taijinar Salt Lake brine. Chem. Engineer. J. 350, 474–483. https://doi.org/10.1016/j.cej.2018.05.191, 2018/10/15/.

Han, G., Gu, D., Lin, G., Cui, Q., Wang, H., 2018. Recovery of lithium from a synthetic solution using spodumene leach residue. Hydrometallurgy 177, 109–115. https://doi.org/10.1016/j.hydromet.2018.01.004, 2018/05/01/.

Han, H., He, Y., Zhang, W., Gu, W., Wu, Y., Tang, W., 2022. Improved adsorption performance and magnetic recovery capability of Al–Fe co-doped lithium ion sieves. New J. Chem. 46 (40), 19230–19240. https://doi.org/10.1039/D2NJ03217A.

Ji, P.-Y., Ji, Z.-Y., Chen, Q.-B., Liu, J., Zhao, Y.-Y., Wang, S.-Z., Li, F., Yuan, J.-S., 2018. Effect of coexisting ions on recovering lithium from high Mg^{2+}/Li^+ ratio brines by selective-electrodialysis. Sep. Purif. Technol. 207, 1–11. https://doi.org/10.1016/j.seppur.2018.06.012, 2018/12/22/.

Ju, S., Xue, F., Qian, J., Chen, F., Wang, B., 2022. Synthesis of Ga^{3+} doped lithium manganese ion sieve for Li^+ extraction and its adsorption thermodynamic behavior. Sep. Sci. Technol. 57 (18), 2923–2936. https://doi.org/10.1080/01496395.2022.2089586, 2022/12/12.

Kölbel, L., Kölbel, T., Herrmann, L., Kaymakci, E., Ghergut, I., Poirel, A., Schneider, J., 2023. Lithium extraction from geothermal brines in the Upper Rhine Graben: a case study of potential and current state of the art. Hydrometallurgy 221, 106131. https://doi.org/10.1016/j.hydromet.2023.106131, 2023/08/01/.

Kang, Y., Xie, Y., Su, F., Dai, K., Shui, M., Shu, J., 2022. α-Li_2TiO_3: a new ultrastable anode material for lithium-ion batteries. Dalton Transac. 51 (47), 18277–18283. https://doi.org/10.1039/D2DT03115A.

Karrech, A., Azadi, M.R., Elchalakani, M., Shahin, M.A., Seibi, A.C., 2020. A review on methods for liberating lithium from pegmatities. Miner. Eng. 145, 106085 https://doi.org/10.1016/j.mineng.2019.106085. /01/01/2020.

Li, R., Wang, Y., Chen, L., Duan, W., Ren, Z., Zhou, Z., 2023. Ionic liquid for selective extraction of lithium ions from Tibetan salt lake brine with high Na/Li ratio. Desalination., 117274 https://doi.org/10.1016/j.desal.2023.117274, 2023/12/29/.

Limjuco, L.A., Nisola, G.M., Lawagon, C.P., Lee, S.P., Seo, J.G., Kim, H., Chung, W.J., 2016. H_2TiO_3 composite adsorbent foam for efficient and continuous recovery of Li^+ from liquid resources. Colloids and Surfaces A: Physicochem. Engineer. Aspects 504, 267–279. https://doi.org/10.1016/j.colsurfa.2016.05.072, 2016/09/05/.

Liu, G., Zhao, Z., Ghahreman, A., 2019. Novel approaches for lithium extraction from salt-lake brines: a review. Hydrometallurgy 187, 81–100. https://doi.org/10.1016/j.hydromet.2019.05.005, 2019/08/01/.

Long, X., Liu, C., Yang, Y., Dong, B., Chen, H., Zhang, L., Pan, J., Zhou, C., 2024. Microwave-assisted hydrothermal synthesis of lithium ion-sieve for adsorption of lithium ion in coal gangue leaching solution. Colloids and Surfaces A: Physicochemical and Engineering Aspects 682, 132819. https://doi.org/10.1016/j.colsurfa.2023.132819, 2024/02/05/.

Marthi, R., Asgar, H., Gadikota, G., Smith, Y.R., 2021. On the structure and lithium adsorption mechanism of layered H_2TiO_3. ACS. Appl. Mater. Interfaces. 13 (7), 8361–8369. https://doi.org/10.1021/acsami.0c20691, 2021/02/24.

Mends, E.A., Chu, P., 2023. Lithium extraction from unconventional aqueous resources – A review on recent technological development for seawater and geothermal brines. J. Environ. Chem. Eng. 11 (5), 110710 https://doi.org/10.1016/j.jece.2023.110710, 2023/10/01/.

Meng, X., Jing, Y., Li, J., Sun, Z., Wu, Z., 2024. Electrochemical recovery of lithium from brine by highly stable truncated octahedral $LiNi_{0.05}Mn_{1.95}O_4$. Chem. Eng. Sci. 283, 119400 https://doi.org/10.1016/j.ces.2023.119400, 2024/01/05/.

Monchak, M., Dolotko, O., Mühlbauer, M.J., Baran, V., Senyshyn, A., Ehrenberg, H., 2016. Monoclinic β-Li_2TiO_3: neutron diffraction study and estimation of Li diffusion pathways. Solid State Sci. 61, 161–166. https://doi.org/10.1016/j.solidstatesciences.2016.09.008, 2016/11/01/.

Noerochim, L., Satriawangsa, G.A., Susanti, D., Widodo, A., 2015. Synthesis and characterization of lithium manganese oxide with different ratio of mole on lithium recovery process from ge-othermal fluid of Lumpur Sidoarjo. J. Mater. Sci. Chem. Engineer. 03 (11), 61374 https://doi.org/10.4236/msce.2015.311007. Vol.No.Art no.

Orooji, Y., Nezafat, Z., Nasrollahzadeh, M., Shafiei, N., Afsari, M., Pakzad, K., Razmjou, A., 2022. Recent advances in nanomaterial development for lithium ion-sieving technologies. Desalination 529, 115624. https://doi.org/10.1016/j.desal.2022.115624, 2022/05/01/.

Qian, F., Zhao, B., Guo, M., Li, J., Liu, Z., Wu, Z., 2020a. K-gradient doping to stabilize the spinel structure of $Li_{1.6}Mn_{1.6}O_4$ for Li^+ recovery. Dalton Transact. 49 (31), 10939–10948. https://doi.org/10.1039/D0DT02405H.

Qian, F., Zhao, B., Guo, M., Qian, Z., Wu, Z., Liu, Z., 2020b. Trace doping by fluoride and sulfur to enhance adsorption capacity of manganese oxides for lithium recovery. Mater. Des. 194, 108867 https://doi.org/10.1016/j.matdes.2020.108867, 2020/09/01/.

Qian, F., Zhao, B., Guo, M., Wu, Z., Zhou, W., Liu, Z., 2021a. Surface trace doping of Na enhancing structure stability and adsorption properties of $Li_{1.6}Mn_{1.6}O_4$ for Li^+ recovery. Sep. Purif. Technol. 256, 117583 https://doi.org/10.1016/j.seppur.2020.117583, 2021/02/01/.

Qian, F., Guo, M., Qian, Z., Zhao, B., Li, J., Wu, Z., Liu, Z., 2021b. Enabling highly structure stability and adsorption performances of $Li_{1.6}Mn_{1.6}O_4$ by Al-gradient surface doping. Sep. Purif. Technol. 264, 118433 https://doi.org/10.1016/j.seppur.2021.118433, 2021/06/01/.

Reich, R., Slunitschek, K., Danisi, R.M., Eiche, E., Kolb, J., 2023. Lithium extraction techniques and the application potential of different sorbents for lithium recovery from brines. Mineral Process. Extrac. Metallur. Rev. 44 (4), 261–280. https://doi.org/10.1080/08827508.2022.2047041, 2023/05/19.

Ryu, T., Shin, J., Ghoreishian, S.M., Chung, K.-S., Huh, Y.S., 2019. Recovery of lithium in seawater using a titanium intercalated lithium manganese oxide composite. Hydrometallurgy 184, 22–28. https://doi.org/10.1016/j.hydromet.2018.12.012, 2019/03/01/.

Shi, X.-c., Zhang, Z.-b., Zhou, D.-f., Zhang, L.-f., Chen, B.-z., Yu, L.-l., 2013. Synthesis of Li^+ adsorbent (H_2TiO_3) and its adsorption properties. Transac. Nonferrous Metals Society China 23 (1), 253–259. https://doi.org/10.1016/S1003-6326(13)62453-X, 2013/01/01/.

Sun, X., Radovanovic, P.V., Cui, B., 2015. Advances in spinel $Li_4Ti_5O_{12}$ anode materials for lithium-ion batteries. New J. Chem. 39 (1), 38–63. https://doi.org/10.1039/C4NJ01390E, 10.1039/C4NJ01390E.

Sun, J., Li, X., Huang, Y., Luo, G., Tao, D., Yu, J., Chen, L., Chao, Y., Zhu, W., 2023. Preparation of high hydrophilic H_2TiO_3 ion sieve for lithium recovery from liquid lithium resources. Chem. Engineer. J. 453, 139485. https://doi.org/10.1016/j.cej.2022.139485, 2023/02/01/.

Swain, B., 2017. Recovery and recycling of lithium: a review. Sep. Purif. Technol. 172, 388–403. https://doi.org/10.1016/j.seppur.2016.08.031, 2017/01/01/.

U.S. Geological Survey (USGS), 2023. Mineral Commodity Summaries 2023. Available at https://pubs.usgs.gov/publication/mcs2023.

Vera, M.L., Torres, W.R., Galli, C.I., Chagnes, A., Flexer, V., 2023. Environmental impact of direct lithium extraction from brines. Nat. Rev. Earth Environ. 4 (3), 149–165. https://doi.org/10.1038/s43017-022-00387-5, 2023/03/01.

Wang, S., Li, P., Cui, W., Zhang, H., Wang, H., Zheng, S., Zhang, Y., 2016. Hydrothermal synthesis of lithium-enriched β-Li_2TiO_3 with an ion-sieve application: excellent lithium adsorption. RSC. Adv. 6 (104), 102608–102616. https://doi.org/10.1039/C6RA18018C.

Wang, S., Zheng, S., Wang, Z., Cui, W., Zhang, H., Yang, L., Zhang, Y., Li, P., 2018a. Superior lithium adsorption and required magnetic separation behavior of iron-doped lithium ion-sieves. Chem. Engineer. J. 332, 160–168. https://doi.org/10.1016/j.cej.2017.09.055, 2018/01/15/.

Wang, S., Chen, X., Zhang, Y., Zhang, Y., Zheng, S., 2018b. Lithium adsorption from brine by iron-doped titanium lithium ion sieves. Particuology 41, 40–47. https://doi.org/10.1016/j.partic.2018.02.001, 2018/12/01/.

Wang, S., Zhang, M., Zhang, Y., Zhang, Y., Qiao, S., Zheng, S., 2019. High adsorption performance of the Mo-doped titanium oxide sieve for lithium ions. Hydrometallurgy 187, 30–37. https://doi.org/10.1016/j.hydromet.2019.05.004, 2019/08/01/.

Wang, L., Wang, L., Wang, J., Wang, X., 2022. Synthesis of zirconium-coated lithium ion sieve with enhanced cycle stability. Sep. Purif. Technol. 303, 121933 https://doi.org/10.1016/j.seppur.2022.121933, 2022/12/15/.

Wang, W., Wang, C., Zhang, Y., Xu, H., Shao, L., 2024. Highly positively-charged membrane enabled by a competitive reaction for efficient Li^+/Mg^{2+} separation. Sep. Purif. Technol. 330, 125428 https://doi.org/10.1016/j.seppur.2023.125428, 2024/02/01/.

Wei, S., Wei, Y., Chen, T., Liu, C., Tang, Y., 2020. Porous lithium ion sieves nanofibers: general synthesis strategy and highly selective recovery of lithium from brine water. Chem. Engineer. J. 379, 122407 https://doi.org/10.1016/j.cej.2019.122407, 2020/01/01/.

Weng, D., Duan, H., Hou, Y., Huo, J., Chen, L., Zhang, F., Wang, J., 2020. Introduction of manganese based lithium-ion Sieve-A review. Progress Natur. Sci.: Mater. Int. 30 (2), 139–152. https://doi.org/10.1016/j.pnsc.2020.01.017, 2020/04/01/.

Xiao, W., Xin, C., Li, S., Jie, J., Gu, Y., Zheng, J., Pan, F., 2018. Insight into fast Li diffusion in Li-excess spinel lithium manganese oxide. J. Mater. Chem. A 6 (21), 9893–9898. https://doi.org/10.1039/C8TA01428K.

Xu, X., Chen, Y., Wang, P., Gasem, K., Wang, K., He, T., Adidharma, H., Fan, M., 2016. Extraction of lithium with functionalized lithium ion-sieves. Prog. Mater. Sci. 84, 276–313. https://doi.org/10.1016/j.pmatsci.2016.09.004, 2016/12/01/.

Xu, R., Lei, S., Wang, T., Yi, C., Sun, W., Yang, Y., 2023. Lithium recovery and solvent reuse from electrolyte of spent lithium-ion battery. Waste Manage. 167, 135–140. https://doi.org/10.1016/j.wasman.2023.05.034, 2023/07/15/.

Yang, L., Gao, Z., Liu, T., Huang, M., Liu, G., Feng, Y., Shao, P., Luo, X., 2023. Direct electrochemical leaching method for high-purity lithium recovery from spent lithium batteries. Environ. Sci. Technol. 57 (11), 4591–4597. https://doi.org/10.1021/acs.est.3c00287, 2023/03/21.

Yu, Q., Sasaki, K., 2016. Microwave-assisted hydrothermal synthesis of nanocrystalline lithium-ion sieve from biogenic manganese oxide, its characterization and lithium sorption studies. Hydrometallurgy 165, 118–124. https://doi.org/10.1016/j.hydromet.2015.10.002, 2016/10/01/.

Zeng, X., Li, M., Abd El-Hady, D., Alshitari, W., Al-Bogami, A.S., Lu, J., Amine, K., 2019. Commercialization of Lithium Battery Technologies for Electric Vehicles. Adv. Energy Mater. 9 (27), 1900161. https://doi.org/10.1002/aenm.201900161.

Zhang, L., Zhou, D., He, G., Wang, F., Zhou, J., 2014. Effect of crystal phases of titanium dioxide on adsorption performance of H_2TiO_3-lithium adsorbent. Mater. Lett. 135, 206–209. https://doi.org/10.1016/j.matlet.2014.07.176, 2014/11/15/.

Zhang, G., Zhang, J., Zhou, Y., Qi, G., Wu, Y., Hai, C., Tang, W., 2019. Synthesis of aluminum-doped ion-sieve manganese oxides powders with enhanced adsorption performance. Colloids and Surfaces A: Physicochem. Engineer. Aspects 583, 123950. https://doi.org/10.1016/j.colsurfa.2019.123950, 2019/12/20/.

Zhang, G., Zhang, J., Zeng, J., Sun, Y., Shen, Y., Li, X., Ren, X., Hai, C., Zhou, Y., Tang, W., 2021. Improved structural stability and adsorption capacity of adsorbent material $Li_{1.6}Mn_{1.6}O_4$ via facile surface fluorination. Colloids and Surfaces A: Physicochem. Engineer. Aspects 629, 127465. https://doi.org/10.1016/j.colsurfa.2021.127465, 2021/11/20/.

Zhang, G., Hai, C., Zhou, Y., Tang, W., Zhang, J., Zeng, J., Liu, Y., Dong, S., Peng, G., 2022. Al and F ions co-modified $Li_{1.6}Mn_{1.6}O_4$ with obviously enhanced Li^+ adsorption performances. Chemical Engineering Journal 450, 137912. https://doi.org/10.1016/j.cej.2022.137912, 2022/12/15/.

Zhang, G., Yuan, X., Tay, C.Y., He, Y., Wang, H., Duan, C., 2023a. Selective recycling of lithium from spent lithium-ion batteries by carbothermal reduction combined with multistage leaching. Sep. Purif. Technol. 314, 123555 https://doi.org/10.1016/j.seppur.2023.123555, 2023/06/01/.

Zhang, J., Cheng, Z., Qin, X., Gao, X., Wang, M., Xiang, X., 2023b. Recent advances in lithium extraction from salt lake brine using coupled and tandem technologies. Desalination. 547, 116225 https://doi.org/10.1016/j.desal.2022.116225, 2023/02/01/.

Zhang, H., Zhang, S., Zhang, W., Ma, W., Li, Y., Chen, L., Zhu, L., Pan, Y., 2023c. Recovering phosphorus and lithium separately from wastewater and brine using a novel coupled biofilm-precipitation system. J. Water. Process. Eng. 55, 104097 https://doi.org/10.1016/j.jwpe.2023.104097, 2023/10/01/.

Zhang, S., Wei, X., Cao, X., Peng, M., Wang, M., Jiang, L., Jin, J., 2024. Solar-driven membrane separation for direct lithium extraction from artificial salt-lake brine. Nat. Commun. 15 (1), 238. https://doi.org/10.1038/s41467-023-44625-w, 2024/01/03.

Zhou, Q., Oya, Y., Chikada, T., Zhang, W., Xue, L., Yan, Y., 2017. Preparation of Li_2TiO_3 by hydrothermal synthesis and its structure evolution under high energy Ar^+ irradiation. J. Eur. Ceram. Soc. 37 (15), 4955–4961. https://doi.org/10.1016/j.jeurceramsoc.2017.06.032, 2017/12/01/.

Zhou, S., Guo, X., Yan, X., Chen, Y., Lang, W., 2022. Zr-doped titanium lithium ion sieve and EP-granulated composite: superb adsorption and recycling performance. Particuology 69, 100–110. https://doi.org/10.1016/j.partic.2021.12.002, 2022/10/01/.

Prof. Bing-Jie Ni received his Ph.D. degree in environmental engineering in June 2009. He currently is a full professor in environmental engineering at the University of New South Wales. He currently serves as Editor, Guest Editor or Editor Board for top journals such as Sustainable Horizons, Water Research, Environmental Science and Technology. He is a Clarivate Highly Cited Researcher. His-work focuses on the integration of different disciplines to develop innovative and sustainable technological solutions to achieve environmental and energy sustainability.